Citation: Rahman, B. M., Rahman, M. M., Sriratanavaree, S., Kejalakshmy, N. & Grattan, K. T. V. (2014). Rigorous analysis of the transverse acoustic modes in optical waveguides by exploiting their structural symmetry. Applied Optics, 53(29), pp. 6797-6803. doi: 10.1364/ao.53.006797

This is the accepted version of the paper.

This version of the publication may differ from the final published version.

Permanent repository link: https://openaccess.city.ac.uk/id/eprint/12227/

Link to published version: https://doi.org/10.1364/ao.53.006797

Rigorous analysis of the transverse acoustic modes in optical waveguides by exploiting their structural symmetry

B. M. A. Rahman,* M. M. Rahman, S. Sriratanavaree, N. Kejalakshmy, and K. T. V. Grattan

Department of Electrical and Electronic Engineering,
City University London, Northampton Square, London, EC1V 0HB, UK

compiled: July 7, 2014

A full-vectorial finite element based approach has been developed to find accurate modal solutions of acoustic modes in Ge-doped planar silica waveguides. The structural symmetry is exploited and Aitken's extrapolation is also used to improve the accuracy of the solution. The spatial dependences of the dominant and non-dominant displacement vectors are shown for the fundamental and higher order transverse modes. The modal hybridness and modal birefringence between the two fundamental transverse modes are also presented.

OCIS codes: (350.7420); (230.7370); (080.1753).

1. Introduction

Acoustic waves propagate inside a waveguide due to the periodic displacement of the molecules and these propagation properties can be characterized by the material density, elasticity, Young's modulus, and Poisson's ratio [1]. The particle displacement can either be in the longitudinal direction or in the transverse plane. An acoustic mode can be supported in a waveguide provided that at least one of the velocities (the shear or longitudinal velocities) in the cladding exceeds that of the core and the propagation of such a mode can be classified as being of the torsional, bending, rotational or longitudinal type [2,3].

It is well known that the acoustic waves in optical waveguides interacts with the propagation of light through the related phenomena of Brillouin Scattering (BS), Stimulated Brillouin Scattering (SBS) and Guided Acoustic Wave Brillouin Scattering (GAWBS) [4-6]. The analyses of such interactions are not trivial, especially with the increased complexity of modern optical waveguide structures, such as micro-structured optical fibers [6] and sub-wavelength silicon nanowires. It is well known [7] that modes in optical waveguides with two-dimensional confinement are hybrid in nature, similar to the acoustic modes in acoustic waveguides, which are shown here to be also hybrid in nature. Most of the optical materials considered are isotropic; however some materials such as lithium niobate is anisotropic. On the other hand, most of the acoustic materials have very different longitudinal and transverse wave velocities, which essentially causes them to be equivalent to having anisotropic acoustic indices. In these cases, a rigorous full-vectorial analysis [8-10] is required for the accurate characterization of the acoustic wave propagation. For this work, a numerical approach based on the powerful and versatile Finite Element Method (FEM) has been developed [11], which can be applied for the analysis of arbitrarily shaped both weakly and strongly guiding acoustic waveguides.

Silica optical fibers are the most extensively used optical waveguides because of their wide availability and extremely low optical loss and their planar versions are also widely used for the fabrication of various planar photonic integrated circuits (PICs). In this paper, modal solutions of transverse acoustic modes of a Ge-doped planar silica waveguide are presented.

2. Theory

The propagation of an acoustic wave along the axial direction, taken here as the z-axis, is associated with the molecular displacement, $\mathbf{U}_i$, and a time harmonic wave can be written in the following form [9]:

$$\mathbf{U}_i = \mathbf{u}\left(u_x, u_y, ju_z\right)\mathbf{exp}[j\left(\omega t - kz\right)]. \qquad (1)$$

---

* Corresponding author: B.M.A.RAHMAN@CITY.AC.UK

where the angular frequency, ω, identifies the time dependence; the propagation constant, k identifies the axial dependence of the acoustic wave and u_x, u_y and u_z are the particle displacement vectors along the x, y and z directions, respectively. For a loss-less system, u_z (the longitudinal component) is 90° out of phase with the two transverse components, u_x and u_y. In this case, by defining u_z as an imaginary component, as shown in Eq. (1), the system equation can be transformed to a much simpler real eigenvalue equation. The deformation in an acoustically vibrating body can be described by the strain field, $\mathbf{S}$, given by:

$$\mathbf{S} = \nabla \mathbf{u}. \tag{2}$$

The elastic restoring forces can be defined in terms of the stress field, $\mathbf{T}$ and the inertial and elastic restoring forces in a freely vibrating medium are related through the translational equation of motion where:

$$\nabla \mathbf{T} = \rho \frac{\partial^2 \mathbf{u}}{\partial t^2}. \tag{3}$$

Hooke's Law states that the strain and stress are linearly proportional to each other and are given by:

$$T_{ij} = c_{ijkl} S_{kl}. \tag{4}$$

here, the microscopic spring constants, c_{ijkl}, are called the elastic stiffness constants. The compliance and stiffness tensors can be denoted in matrix form as:

$$[T] = [c]\,[S]\,. \tag{5}$$

in which c_{ijkl} is the fourth order tensor which obeys the symmetry condition and hence can be represented by using two suffix notations. Furthermore, the elastic stiffness constants are related to the shear and longitudinal velocities.

By substituting Eqs. (2) and (5), Eq. (3) can be transformed to a wave equation with u as the only variable. Classically, in the FEM [12] for a solid structure, the displacement field, $\mathbf{u}$, can be written with the help of the interpolation shape function and its spatial derivatives and integrations can be easily carried out over the elements. The wave equation associated with the acoustic wave propagation can be developed by employing powerful Galerkin approach and minimizing the energy functional, a corresponding eigenvalue equation can be formed, which is given as:

$$\left([A] - \omega^2\,[B]\right)\mathbf{U} = \mathbf{F}. \tag{6}$$

where $[A]$ is the stiffness matrix, related to strain energy and $[B]$ is the mass matrix related to the kinetic energy. These matrices are generated for a given propagation constant, k. The column vectors, $\mathbf{F}$, contain the nodal values of the applied forces, which in this case are taken to be equal to zero. Solving this generalized eigenvalue equation of the system yields the eigenvalue as ω^2, where ω is the acoustic angular frequency and the eigenvector $\mathbf{U}$, the displacement vector. From a given input, k, and its corresponding output, ω, the phase velocity of the acoustic wave, v, can be calculated from:

$$v = \omega / k. \tag{7}$$

However, if it is necessary to calculate the propagation constant for a given frequency, a simple iterative approach can be considered. Numerically efficient computer code has been developed by using the sparse matrix solver along with the versatile mesh generation for an arbitrary shaped waveguide and modal solutions of acoustic modes in practical optical waveguides can be obtained.

3. Results

Silica fibers are the most commonly used optical waveguides due to their property of having the lowest loss so far shown by any optical waveguide and millions of kilometers have been laid down for long-distance communication networks. However, when various photonic components are considered for modern communication systems, often planar forms are used as functionality of a PIC can be increased for a compact, reliable and yet low-cost systems. Although, in the fabrication of PICs, semiconductor materials like InP or GaAs have the advantages of allowing the incorporation of active components such as semiconductor lasers or alternatively electro-optic dielectric materials such as lithium niobate for high-speed modulators, however, for many passive devices such as power splitters and AWG filters, often planar silica guides are used as they have lower loss and cost less and also they provides lower coupling loss to a silica fiber.

Often silica can be doped by Ge to increase the refractive index to form a waveguide core, and this process also increases equivalent acoustic index of the doped region compared to un-doped silica cladding and as a result, this optical waveguide will also supports acoustic waves. The longitudinal and shear acoustic wave velocities of the un-doped silica cladding are taken as, $V_{LC} = 5933$ m/s and $V_{SC} = 3764$ m/s, respectively. Similarly, the longitudinal and shear wave velocities in for 3% Ge-doped core are taken as $V_{LG} = 5806$ m/s and $V_{SG} = 3677$ m/s, respectively [13]. Here the densities of the both doped and undoped silica are taken as 2202 kg/m^3. This waveguide will support both the longitudinal modes and transverse modes. In this work, however our study has been focused on the transverse modes only, which have more complex spatial variations. The acoustic waveguide is illustrated in Fig.1, and its height and width are shown as H and W. It can be observed here that this waveguide has a two-fold symmetry and this symmetry can be exploited, as is discussed later.

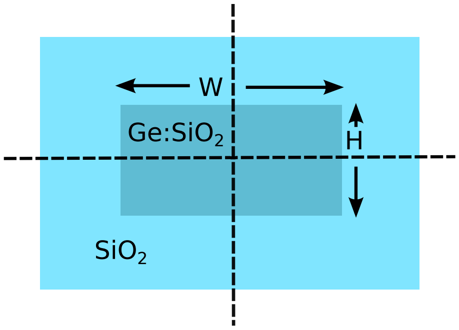

Fig. 1. Ge-doped planar Silica waveguide.

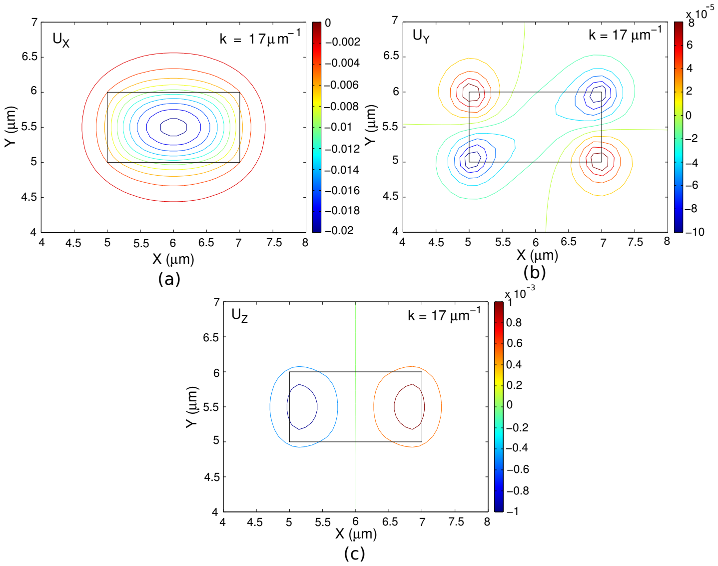

Fig. 2. U_x, U_y and U_z displacement vectors of the U_{11}^x mode.

This waveguide supports two near degenerate fundamental transverse modes. In a way similar to that for optical modes, one of the modes has dominant U_x component and other has a dominant U_y component and these will be identified as U_{mn}^x and U_{mn}^y modes, respectively, where m and n will identify their spatial variations. However, these modes also have other two non-dominant components, such as the U_{mn}^x mode, which will also have U_y and U_z displacement vectors. This confirms that even for a transverse mode, there will be a material displacement along the axial direction also. So, any scalar approach would be unsuitable to find acoustic modes in such a waveguide. The U_x, U_y and U_z displacement vector profiles of the fundamental U_{11}^x mode at $k = 17.0$ μm^{-1} are shown in Fig.2 when the waveguide width, W = 2 μm and its height, H = 1 μm. The outline of the waveguide is shown by solid black lines in the figure. It can be observed that the dominant U_x profile of this mode, shown in Fig.2a, is nearly Gaussian in shape with its peak value at the center of the waveguide. On the other hand, the non-dominant U_y vector as shown in Fig.2b, shows a higher order spatial variation with alternative positive and negative peaks at the adjacent corners of the waveguide where its peak value is about 2 orders of magnitude lower than that of the dominant displacement vector, U_x. The U_z profile is shown in Fig.2c, which illustrates its positive and negative peaks along the two vertical side walls. Its maximum magnitude is about 5% of the fundamental displacement vector, U_x. In this case 200x200 mesh divisions were used for the full structure and the corresponding acoustic frequency was 10.044952 GHz. Similarly, for the fundamental U_{11}^y mode, its acoustic frequency was 10.048059 GHz for the same wavenumber, $k = 17$ μm^{-1}. As the waveguide width and height were not the same, their eigenfrequencies were not exactly the same but yet very close. For this mode, the dominant U_y displacement vector was Gaussian in shape (but is not shown here) with its spatial variation was similar to that shown in Fig.2a (similar to the dominant U_x of the U_{11}^x mode). For this U_{11}^y mode, its non-dominant U_x displacement has four peaks at the four corners of the waveguide and U_z shows its maximum values at the upper and lower horizontal interfaces (but these are not shown here). The close proximity of two fundamental transverse modes allows these modes to interact and eigenvectors become mixed - this cannot be avoided when the whole structures is simulated as both the eigenmodes appear in close proximity. If a finer mesh division can be used then this mode degeneration will reduce.

The spatial variation of the U_y vector for the same U_{11}^x mode, at $k = 17\ \mu m^{-1}$, but when mesh division is increased to 500x500 is shown in Fig.3a. This shows the degeneration has reduced, as four peaks at four corners of the waveguide are more clearly visible. It can also be observed that their peak magnitudes are nearly equal (their exact values cannot be identified here, but from the numerical data obtained, they have been identified as $+1.2619 \times 10^{-4}$ and -1.2156×10^{-4}, respectively). However, when a lower mesh is used, the four peaks begin to mix and the positive and negative peaks become unequal and the U_y profile transforms to show its peak at the center, as shown in Fig.3b, when the mesh division was reduced to 80x80.

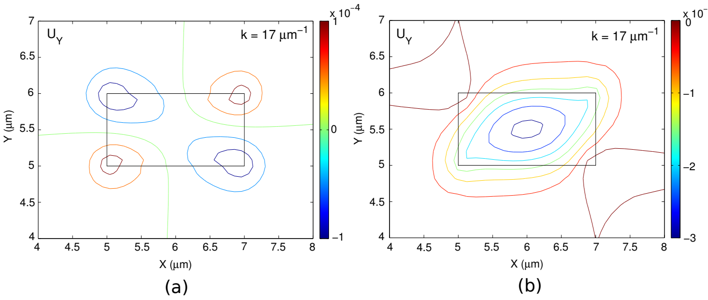

Fig. 3. U_y displacement vectors of the U_{11}^x mode, when (a) 500x500 and (b) 80x80 mesh divisions.

To quantify this mode degeneration, next, the ratio of the minimum peaks with the maximum peaks is shown in Fig.4 with the mesh division used. It can be observed that when a higher mesh division is used, in this case 500x500, the positive and negative peaks were almost equal in magnitude, and their ratio was 0.9633. On the other hand, when a smaller mesh is used, in this case 80x80, the larger peak becomes 8.47 times bigger than the smaller peak, and the profile shows a nearly Gaussian shape with its peak value now at the center of the waveguide as shown in Fig.3b. It can be stated that the U_{11}^x and U_{11}^y modes are mixing up at a progressive rate and non-dominant U_y vector of the U_{11}^x mode is being influenced by the dominant U_y vector of the U_{11}^y mode. When the aspect ratio of the waveguide is increased then this degeneration is reduced as the modal birefringence of the waveguide becomes higher. On the other hand, when the acoustic frequency is reduced, this degeneration is reduced, but not shown here, as the difference between the two similar eigenvalues is increased. However, this modal degeneration between two similar transverse modes cannot be avoided, unless the symmetry of the structures is exploited, as discussed below.

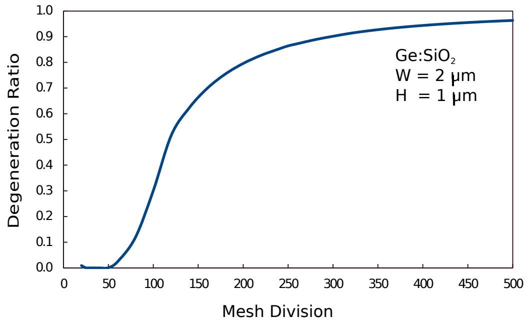

Fig. 4. Degeneration ratio against mesh division for U_y displacement vectors of the U_{11}^x mode.

Symmetry conditions of optical waveguides have been extensively exploited [14], whenever they exist, for the modal solutions of optical waveguides. This not only can avoid mode degeneration by separating two interacting modes, but also allow much improved solutions, with a given computer resource. Since this structure has a two-fold symmetry, only one-quarter of the waveguide needs to be considered, which will allow a much finer mesh division to be used. The combinations of $\mathbf{n} \times \mathbf{U}$ and $\mathbf{n}.\mathbf{U}$ at the vertical and horizontal symmetry lines can be used, and there are 4 combinations, which will give all the U_{mn}^x and U_{mn}^y modes, with various combinations of m and n values, being them odd or even.

Besides the exploitation of the symmetry condition (if it exists), Aitken's extrapolation [15] technique can also be used to improve the solution accuracy. To exploit this, the structure must be refined in a fixed geometric ratio. From three successive mesh refinements, final solutions can be extrapolated for a possible infinite mesh refinement as given here:

$$\omega_\infty = \omega_3 - \frac{(\omega_3 - \omega_2)^2}{\omega_3 - 2\omega_2 + \omega_1}. \qquad (8)$$

where, ω_1, ω_2, and ω_3 are results obtained by successively using higher mesh divisions and ω_∞ is the extrapolated result equivalent to infinite mesh divisions. Here, this geometric ratio does not have to be 1:2:4 but other ratio can also be used, but it should be noted that mesh divisions can only be of integer value and in all the regions the same mesh refinement ratio must be maintained.

Variations of the acoustic frequency of the fundamental U_{11}^x mode for $k = 17\ \mu m^{-1}$ with the mesh division are shown in Fig.5, for both the full and quarter (exploiting the two-fold symmetry) structures. In this case, equal mesh divisions are used in both the transverse directions. It can be noted that as the number of the mesh division is increased, these solutions rapidly converge to their exact solutions. However, it can be easily observed that when 2-fold symmetry is used, as shown by a dotted green line, convergence is much faster than when the full structure is simulated as shown by a dashed blue line. The solution accuracy which can be obtained by a 50x50 mesh divisions for 2-fold symmetry will have the similar accuracy as that of using a 100x100 mesh for the full structure, but requiring a much higher computational resources. Besides that, when Aitken's extrapolation is used, the solution accuracy is much improved as shown by dashed red line. For the full structure, when the geometric ratio 1:2:4 and 1:1.5:2.25 (or 4:6:9) are used, as identified as ATF(1:2:4) and ATF(4:6:9), and shown by the red dashed and yellow solid lines, respectively, it can be observed that better solution accuracy can be obtained. However, it can be noted that 4:6:9 geometric ratio, shown by a yellow solid line, converges better than use of 1:2:4 (dashed red line). On the other hand, when the 4:6:9 geometric ratio for the quarter structure (exploiting 2-fold symmetry), as shown by a dashed cyan line (ATT(4:6:9)), best solution convergence can be obtained, for a given mesh division as here both symmetry and extrapolation have been used. To show this region more clearly, an expanded version of this region is shown as an inset.

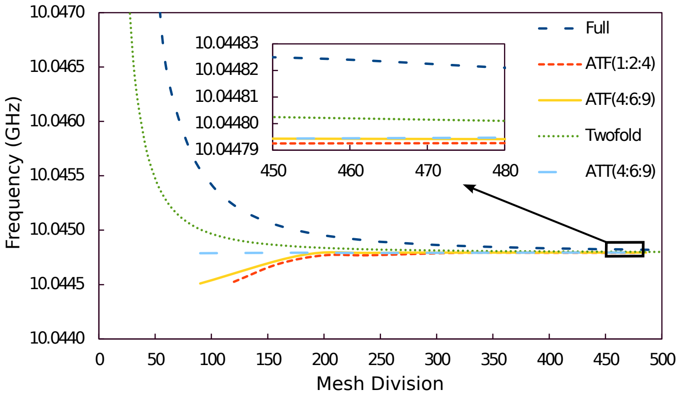

Fig. 5. Variation of eigen frequency with the mesh division for the U_{11}^x mode at $k = 17\ \mu m^{-1}$.

Following the clear demonstration of the advantages of exploiting symmetry conditions and also that of using the Aitken's extrapolation, dispersion curves of all the transverse U_{mn}^x modes are calculated for a 2 $\mu m \times 1\ \mu m$ Ge-doped silica waveguide and shown in Fig.6. The variations of their phase velocities with the acoustic frequencies are shown here. For the fundamental U_{11}^x mode, as shown by a blue line, it can be observed that when the frequency is reduced the phase velocity increases monotonically and reaches that of the cladding shear velocity, V_{CS}, as the mode approaches its cutoff near 3.59 GHz. It was noted that as the frequency is increased the mode becomes more confined within the core. The full-width-half-maximum (FWHM) of the displacement vectors has been calculated. The FWHM for the U_{11}^x mode in the x-direction was 2.9 μm at $f = 4$ GHz and this value reduces to 1.5 μm when the frequency increases to 16 GHz. For this waveguide, the cutoff frequency of the second mode, U_{21}^x, shown by a red line is 7.19 GHz, so this waveguide will support only one transverse mode (with the dominant U_x displacement) between 3.6-7.2 GHz. It should also be noted that the dispersion curves for the U_{12}^x and U_{21}^x are different as the height and width of the waveguide were not the same. Even when the height and width of a waveguide are equal (the waveguide has a 90° rotational symmetry), the U_{21}^x and U_{12}^x modes would be degenerate but by exploiting the symmetry conditions, as shown here, they can be isolated. It should be noted that similar dispersion curves for all the U_{mn}^y modes can also be obtained. However, it should be noted that for identical height and width, U_{12}^x and U_{21}^y will have the same eigenfrequency and as they also require the same symmetry conditions they cannot be isolated.

Although, the spatial variation of the dominant displacement vector can be easily identified or visualized, there has, however not been much reported on the spatial variations of the other two non-dominant displacement vectors for the same mode. Rather, in many cases, a simpler

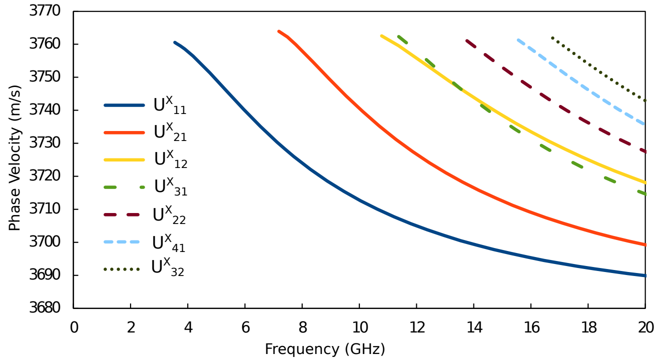

Fig. 6. Dispersion curves of acoustic shear U^x_{mn} modes.

scalar formulation has been used [16] to find the modal solutions of the acoustic modes, where the non-dominant components are totally neglected. For a higher order U^x_{21} mode the spatial variation of the two non-dominant components, U_y and U_z are shown in Fig.7. The U_x profile for this mode is not shown, but this has two well defined half-wave variations (m=2) along the x-direction and one half-wave variation (n=1) along the y-direction. The U_y profile for the same mode is shown in Fig.7a, which identifies 3 half-wave (m+1) variations along the x-direction, and 2 half-wave (n+1) variations along the y-direction. It has been verified that this relation for the spatial variation of the non-dominant transverse component holds true for all the U^x_{mn} modes with m+1 and n+1 half-wave variations along the x and y-directions. This can also be confirmed for the U^x_{11} mode as shown in Fig.2. Similarly the U_z profile for the U^x_{21} mode, shown in Fig.7b, shows 3 (=m+1) and 1 (=n) half-wave variations along the x- and y directions, and the same relations has been checked to be true for all U^x_{mn} modes. The spatial variations of the non-dominant U_x displacement vector for the U^y_{mn} modes is not shown here. However, it has been identified during this study that, for these modes it is the non-dominant transverse component, U_x which will have m+1 and n+1 half-wave variations along the x and y-directions, and its U_z component will have m and n+1 half-wave variations along the x and y-directions, as shown in Fig.7c for the U^y_{21} mode.

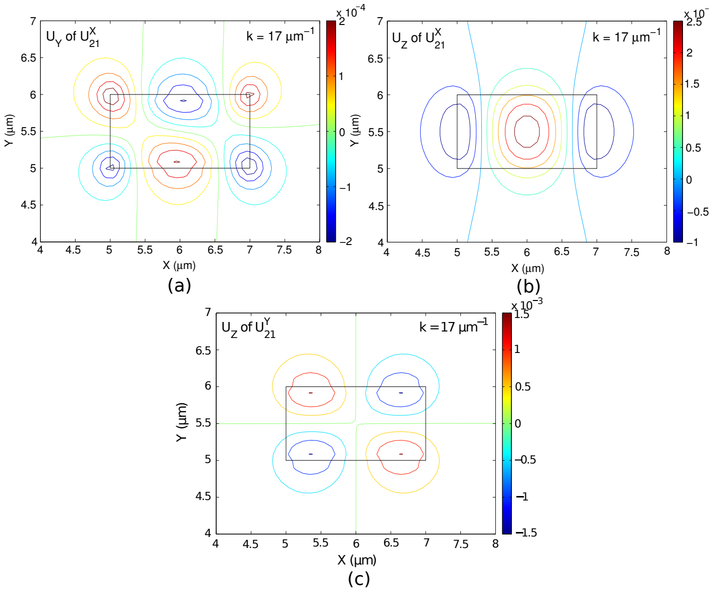

(a) (b)

(c)

Fig. 7. Displacement fields (a)U_y,(b)U_z of U^x_{21} and (c)U_z of U^y_{21} modes.

In this study it is shown here that the acoustic modes are fully vectorial in nature and for a transverse mode, although its dominant displacement is along one of the transverse direction, however, other two non-dominant (another one transverse and one longitudinal) are also present. This makes the modes fully hybrid in nature. Similarly, modes in optical waveguides with 2-dimensional confinements are also fully hybrid in nature and this hybridness increases when the index contrast between core and cladding is increased. A study of modal hybridness is important for the calculation of polarization cross-talk [17] or in the design of polarization rotators [18]. Hybridness can be defined as the ratio of the maximum value of the non-dominant component with the maximum value of the dominant components. As for each mode, there are two non-dominant components, so there will be two different hybridness values for each of the modes; however, the ratio between the longitudinal and transverse components is of greatest interest.

For the U^x_{11} and U^y_{11} modes, the variations of the hybridness with the acoustic frequency are shown in Fig.8. Here the hybridness for the transverse modes has been defined as the ratio of the maximum U_z vector to the maximum transverse displacement, which are U_x and U_y for the U^x_{11} and U^y_{11} modes, respectively. It can be observed that as the frequency is decreased modal hybridness increases and reaches its maximum value and then reduces as the modes approach their cutoff frequencies. The modal hybridness of the U^x_{11}, U^y_{21}, and U^x_{31} modes are shown in Fig.9. It can be observed that modal hybridness of the higher order modes are higher than that of the fundamental mode.

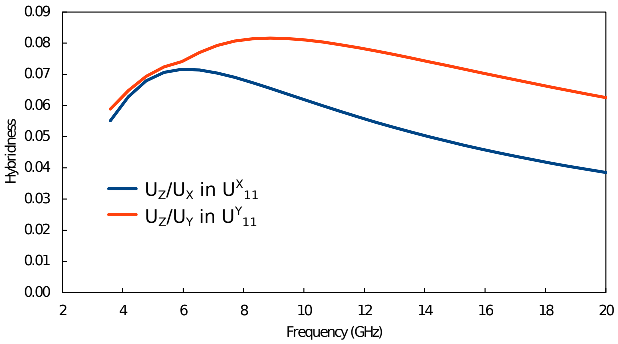

Fig. 8. Variation of modal hybridness of two fundamental transverse modes with the frequency

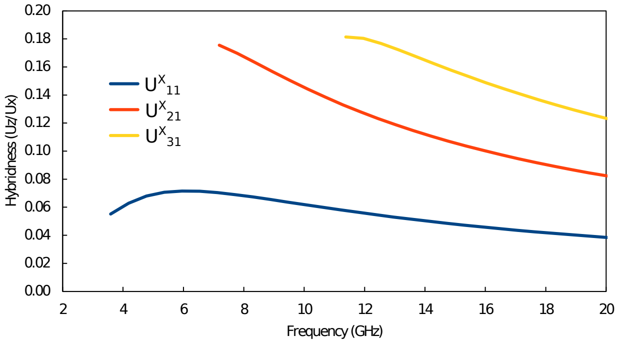

Fig. 9. Variation of the modal hybridness for the higher order modes.

As the waveguide under consideration, with W $= 2\ \mu m$ and H$= 1\ \mu m$, does not have a 90° rotational symmetry so the propagation velocities of the fundamental U^x_{11} and U^y_{11} modes were although close but not identical. For an optical waveguide the difference between the effective indices of the 2 polarized quasi-TE and quasi-TM modes is known as the modal birefringence. Similarly, here the phase velocities of the U^x_{11} and U^y_{11} modes are slightly different. The variation of this modal birefringence (but defined here in terms of their phase velocity difference) with the acoustic frequency is shown in Fig.10 by a blue line for the above waveguide. As the frequency is reduced, difference in their phase velocity increases, reaches a maxima, and then decreases. Subsequently another waveguide is studied where Ge-doping is increased to 6%, so that the difference between the shear velocities in the core and cladding, $\triangle V_S = V_{SG} - V_{SC}$, is now double. The variation of phase velocity difference for this guide is shown by a solid red line. In a way similar to that seen in optical waveguides, the modal birefringence is increased as the equivalent acoustic index contrast between core and cladding is increased. The peak birefringence appears at a lower frequency as with higher index contrast the modal cutoff point is also shifted to a lower frequency.

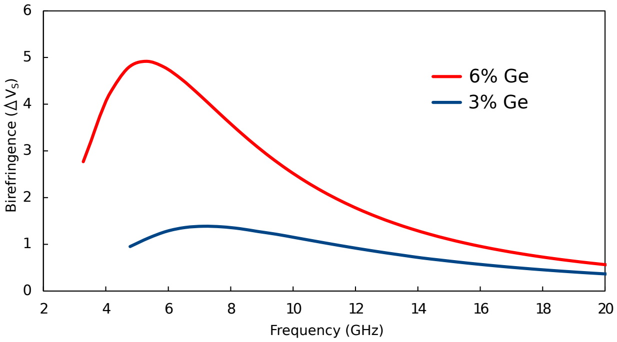

Fig. 10. Variation of modal birefringence with frequency for different Ge doped waveguides.

4. Conclusions

A rigorous full-vectorial acoustic mode solver has been developed by using computationally efficient finite element method. In this work, the advantages of using the symmetry conditions and the type of symmetry walls which can be used are discussed. It is also shown that by using Aitken's extrapolation the solution accuracy can also be improved with the use of finite computer resources. The spatial variations of the dominant and non-dominant displacement vectors of the acoustic modes are also shown here.

It is shown here that Ge:doped planar silica waveguide can support transverse acoustic modes. The co-guidance of the acoustic and optical mode will give rise to SBS above a certain threshold power. This can be detrimental as this would limit high power delivery through this waveguide. On the other hand this can be exploited in the design of compact temperature and pressure sensors. Although, the longitudinal modes are not shown here, this waveguide will also support this class of modes. All these modes may have either dominant transverse or longitudinal component but also two other non-dominant components. The optical modes in a waveguide with two-dimensional confinement are also hybrid in nature, and the modal hybridness increases when index contrast is increased. To study the complex interaction between the fully hybrid acoustic modes and optical modes, a full vectorial approach needs to be used, as shown here. The numerical approach presented here can be used for a wide range of practical optical waveguides with either co- or anti-guiding acoustic modes to study their acousto-optical interactions.

References

[1] B. A. Auld, *Acoustic Fields and Waves in Solids* (John Wiley & Sons, 1973), Chaps. 1-3.

[2] R. N. Thurston, "Elastic waves in rods and clad rods," J. Acoust. Soc. Am. **64**(1), 1-37 (1978).

[3] A. Safaai-Jazi, "Acoustic modes in optical fiber like waveguides," IEEE Trans. Ultrason. Ferroelectr. Freq. Control **35**(5), 619-627 (1988).

[4] G. P. Agrawal, *Nonlinear Fiber Optics* (Academic, 2007), Chap. 9.

[5] R. M. Shelby, M. D. Levenson, and P. W. Bayer, "Guided acoustic wave Brillouin scattering," Phys. Rev. B, **31**(8), 5244-5252 (1985).

[6] P. Dainese, P. St. J. Russell, N. Joly, J. C. Knight, G. S. Wiederhecker, H. L. Fragnito, V. Laude, and A. Khelif, "Stimulated Brillouin scattering from multi-GHz-guided acoustic phonons in nanostructured photonic crystal fibers," Nature Phys. **2**, 388-392 (2006).

[7] B. M. A. Rahman and A. Agrawal, *Finite Element Modelling Methods for Photonics* (Artech, 2013), Chap. 2.

[8] M. Koshiba, S. Mitobe, and M. Suzuki, "Finite-element solution of periodic waveguides for acoustic waves," IEEE Trans. Ultrason. Ferroelectr. Freq. Control $\mathbf{UFFC-34}$(4), 472-477 (1987).

[9] P. E. Lagasse, "Higher-order finite-element analysis of topographic guides supporting elastic surface waves," J. Acoust. Soc. Am. **53**(4), 1116-1122 (1973).

[10] G. O. Stone, "High-order finite elements for inhomogeneous acoustic guiding structures," IEEE Trans. Microw. Theory Tech. $\mathbf{MTT-21}$(8), 538-542 (IEEE, 1973).

[11] S. Sriratanavaree, B. M. A. Rahman, D. M. H. Leung, N. Kejalakshmy, and K. T. V. Grattan, "Rigorous characterization of acoustic-optical interactions in silicon slot waveguides by full-vectorial finite element method ", Opt. Express **22**, 9528-9536, (2014).

[12] O. C. Zienkiewicz, *The Finite Element Method* (1977).

[13] C. K. Jen, A. Saffaai-Jazi, and G. W. Farnell, "Leaky modes in weakly guiding fiber acoustic waveguides," IEEE Trans. Ultrason. Ferroelectr. Freq. Control $\mathbf{UFFC-33}$(6), 619-627 (IEEE, 1986).

[14] B. M. A. Rahman and A. Agrawal, *Finite Element Modelling Methods for Photonics* (Artech, 2013), Chap. 3.

[15] B. M. A. Rahman, and J. B. Davies, "Vector-H finite element solution of GaAs/GaAlAs rib waveguide", IEE Proceedings Pt. J. **132**, 349-353 (1985).

[16] S. Yoo, C. A. Codemard, Y. Jeong, J. K. Sahu, and J. Nilsson, "Analysis and optimization of acoustic speed profiles with large transverse variation for mitigation of stimulated Brillouin scattering in optical fibers," Appl. Opt. **49**, 1188-1199 (2010).

[17] N. Somasiri and B. M. A. Rahman, "Polarization crosstalk in high index contrast planar silica waveguides with slanted sidewalls," J. Lightwave Technol. **21**, 54-60 (2003).

[18] B. M. A. Rahman, S. S. A. Obayya, N. Somasiri, M. Rajarajan, K. T. V. Grattan, and H. A. El-Mikathi, "Design and characterization of compact single-section passive polarization rotator," J. Lightwave Technol. **19**, 512-519 (2001).